CARBON letters

Original Articles
Carbon Letters Vol. 28, 38-46 (2018)

Pyrolysis kinetics and microstructure of thermal conversion products on toluene soluble component from two kinds of modified pitch

Yaming Zhu, Xuefei Zhao♠, Lijuan Gao, and Junxia Cheng

Engineering Research Center of Advanced Coal Coking and Efficient Use of Coal Resources, University of Science and Technology Liaoning, Anshan 114051, China

Article Info
Received 14 July 2017
Accepted 21 September 2017

♠**Corresponding Author**
E-mail: zhao_xuefei@sohu.com.
Tel: +18341270860

Open Access
DOI: http://dx.doi.org/10.5714/CL.2018.28.038

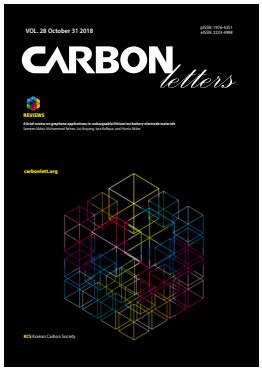

http://carbonlett.org

pISSN: 1976-4251
eISSN: 2233-4998

Abstract

Modified pitch A (MPA) and modified pitch B (MPB) were prepared by oxidative polymerization and thermal polycondensation reaction with refined pitch as the raw material, respectively. The toluene soluble components (TS-1 and TS-2) were obtained by solvent extraction from MPA and MPB, separately. The Flynn-Wall-Ozawa method and Kissinger-Akahira-Sunose method were used to calculate the pyrolysis activation energy of TS. The Satava-Sestak method was used to investigate the pyrolysis kinetic parameters of TS. Moreover, the optical microstructure of the thermal conversion products (TS-1-P and TS-2-P) by calcination shows that TS-1-P has more contents of mosaic structure and lower contents of fine fiber structure than TS-2-P. The research result obtained by a combination of X-ray diffraction and the curve-fitting method revealed that the ratios of ordered carbon crystallite (Ig) in TS-1-P and TS-2-P were 0.3793 and 0.4417, respectively. The distributions of carbon crystallite on TS-1-P and TS-2-P were calculated by Raman spectrum and curve-fitting analysis. They show that the thermal conversion product of TS-2 has a better graphite crystallite structure than TS-1.

Key words: modified pitch, toluene soluble component, thermal conversion, microstructure

1. Introduction

Coal tar pitches have attracted considerable attention in recent decades. They are key precursor materials of a wide range of engineering carbon and graphite materials due to their high carbon content [1,2]. Coal tar pitch has widely used to produce needle coke [3-5], carbon fiber [6,7], and mesocarbon microbeads [8]. Researchers have reported that coal tar pitch is one of the preconceived raw materials to produce condensed poly-nuclear aromatic resin [9-12]. However, coal tar pitches without the removal of quinolone insoluble (QI) is not suitable to produce such high-quality carbon materials. Generally, refined pitches (the QI in coal tar pitch has been removed) is used as the raw material, and several methods have been used to modify coal tar pitches, including mild oxidation by air blowing [13-15], thermal treatment [16,17], chemical additives, and catalytic reactions [18,19].

Thermal treatment and oxidation by air blowing are typical methods to prepare modified pitches. Obviously, the structure and properties of the modified pitches vary according to the modification methods applied. A series of characterization methods have been used to identify the properties of various pitches, such as proximate analysis, elemental analysis, FTIR, ^{1}H-NMR, ^{13}C-NMR, TG/DTG analysis, and so forth [20-23]. However, there has been less study of the pyrolysis characteristics of various pitches. Moreover, there have been very few reports on the microcrystalline structure analysis of calcinated thermal conversion products

Table 1. Proximate analysis of pitch samples

Sample	SP[a] (°C)	TI[b] (wt%)	QI[c] (wt%)	CV[d] (wt%)	β Resin[e] (wt%)	Ash (%)
Refined pitch	49	10.95	0.07	41.76	10.88	0.005
Modified pitch A	232	53.16	30.18	52.33	22.98	0.064
Modified pitch B	228	60.29	25.39	81.88	34.90	0.072

[a]Softening point.
[b]Toluene insoluble.
[c]Quinoline insoluble.
[d]Coke value.
[e]TI-QS.

from various pitches.

For a detailed analysis of the pyrolysis characteristics of modified pitches prepared by thermal treatment and oxidation by air blowing, the toluene soluble (TS) of modified pitches were examined by TG/DTG analysis. Three methods, namely, Flynn-Wall-Ozawa (FWO), Kissinger-Akahira-Sunose (KAS), and Satava-Sestak (SS) were used to calculate the kinetics parameters. In addition, the carbon microcrystalline structure of thermal conversion products of low-temperature calcination from TS were quantitatively analyzed by polarizing microscopy, X-ray diffraction (XRD), and the Raman spectrum and curve-fitting method in this work.

2. Experimental

2.1. Production and properties of TS

The samples TS-1 and TS-2 were obtained from modified pitch A (MPA) and modified pitch B (MPB) by the extraction method with toluene as the solvent. Refined pitch prepared from medium pitch was used as the raw material for preparing the modified pitches. Briefly, MPA was obtained by air oxidation treatment in a stainless-steel reactor. It was heated to 280˚C at the heating rate of 5˚C/min; the holding time was 6 h, and air was used as the oxygen supply agent. The modification method of thermal treatment was used to prepare MPB. Briefly, 100 g of refined pitch was heated to 420˚C at the heating rate of 5˚C/min; the holding time was 4 h, and N_2 was used as the inert gas. The proximate analysis results of the refined pitch and modified pitches are shown in Table 1. The ultimate analysis of TS was done by using a Vario EL Ⅲ elemental analyzer (Elementar, Germany). The oxygen content was calculated by various methods, and the results are shown in Table 2.

Table 2. Ultimate analysis of samples

Sample	C (%)	H (%)	N (%)	S (%)	O (%)
TS-1	92.25	4.03	0.90	0.88	1.94
TS-2	93.75	3.70	0.83	0.68	1.04

2.2. Preparation of thermal conversion products

The thermal conversion products (TS-1-P and TS-2-P) were obtained under certain conditions. Briefly, 20 g of TS was put into a glass tube and transferred to the tube furnace. Then it was heated to 723 K (500˚C) at the heating rate of 2 K min^{-1} with a holding time of 5 h. The thermal conversion products were calcinated at the temperature of 1273 K (1000˚C) for 1 hour at the heating rate of 5 K min^{-1} in a resistance furnace.

2.3. TG/DTG analysis of TS

The pyrolysis characteristic of TS was examined by thermogravimetric analysis (TAQ500, TA Instrument Co., America) under a high-purity N_2 flow rate of 100 mL min^{-1}. Non-isothermal experiments were performed at the temperature range between room temperature and 900 K at the heating rates of 5, 7.5, 10, and 15 K min^{-1}. The FWO, KAS, and Satava-Sestak methods were used to investigate the pyrolysis kinetics of TS.

2.4. Kinetic approach

The kinetic investigations were based on time and temperature resolved datasets of the conversion (α). In the TG/DTG data, α is defined as [24]

$$\alpha = \frac{m_0 - m_t}{m_0 - m_\infty}, \quad (1)$$

where m_0, m_t, and m_∞ are the initial mass, the mass at time t, and the final mass of the sample after reaction, respectively.

It has been reported that the FWO and KAS methods have the advantage of calculation of activation energy without the prior knowledge of the kinetics mechanism. The equations of the FWO and KAS methods are expressed as follows [24-27]:

$$\text{FWO method: } \lg\beta = \lg\frac{AE}{g(\alpha)R} - 2.315 - 0.4567\frac{E}{RT}, \quad (2)$$

$$\text{KAS method: } \ln\frac{\beta}{T^2} = \ln\frac{AR}{g(\alpha)E} - \frac{E}{RT}. \quad (3)$$

Here, β denotes the heating rate (K min^{-1}), A is the pre-exponential factor (min^{-1}), E is the activation energy (KJ mol^{-1}), R is the universal gas constant (8.314 J/mol K^{-1}), and g (α) is the integral rate equation. To calculate the kinetic param-

Table 3. Forty-one thermal decomposition mechanism functions

No.	Function	Mechanism	g(α)
1	Parabola law	One-dimensional diffusion	α^2
2	Valensi equation	Tne-dimensional diffusion	α+(1-α)ln(1-α)
3-6	Jande equation	Two-dimensional diffusion or three-dimensional diffusion	$[1-(1-\alpha)^m]^n$ (m=1/2, 1/3; n=2, 1/2)
7	G-B equation[a)]	Three-dimensional diffusion	$1-2\alpha/3-(1-\alpha)^{2/3}$
8	Anti-Jande equation	Three-dimensional diffusion	$[(1+\alpha)^{1/3}-1]^2$
9	Z-L-T equation[b)]	Three-dimensional diffusion	$[(1-\alpha)^{1/3}-1]^2$
10-20	Avrami-Erofeev equation	Assumes random nucleation and its subsequent growth	$[-\ln(1-\alpha)]^n$ (n=1/4, 1/3, 1/2, 2/3, 3/4, 3/2, 1, 2, 3, 4)
21	P-T equation[c)]	Auto catalysis, branch random nucleation	ln[α/(1-α)]
22-27	Maple power law	Phase boundary reaction	α^n (n=1/4, 1/3, 1/2, 1, etc.)
29,30	Contracting	Phase boundary reaction	$[1-(1-\alpha)^n]/n$ (n=1/3, 3)
30,31	Contracting cylinder	Phase boundary reaction	$[1-(1-\alpha)^n]/n$ (n=1/2, 2)
28,41 32-38	Reaction order		$1-(1-\alpha)^n$ (n=1/4, 2, 3, 4, 2/3, etc.)
39,40	Exponent law		$\lvert 1n\alpha^n\rvert$ (n=1, 2)

[a)]Ginstling-Brounshtein equation.
[b)]Zhuralev-Lesokin-Tempelman equation.
[c)]Prout-Tompkins equation.

eters and determine the reaction order and mechanism, the Satava-Sestak method [28] was preferred, and the equation is written as

$$\lg g(\alpha) = \lg\frac{AE}{R\beta} - 2.315 - 0.4567\frac{E}{RT}. \quad (4)$$

As described in [29], there are 41 types of thermal decomposition mechanism functions (shows in Table 3) that have been used to determine the reaction mechanism. The reaction mechanism and order are predefined in the Satava-Sestak method. The thermal decomposition mechanism of TS in the conversion range of 0.2≤α≤0.8 was evaluated.

2.5. Characterization of thermal conversion products

The microstructures of TS-1-P and TS-2-P were quantitatively studied in detail by various methods. Obviously, the distribution on the optical microstructure of the calcined thermal conversion products was determined by polarizing microscopy (Axio Scope A1 pol, Carl Zeiss, German). The optical microstructure observations are summarized in Table 4.

XRD analysis (PANalytical X'Pert Powder, the Netherlands) and the curve-fitting method were used to estimate the content of ordered carbon microcrystalline structure. Similarly, Raman spectrum (LabRAM HR Evolution, JOBIN YVON, France) coupled with the curve-fitting method were used to determine the distribution and content of the series carbon microcrystalline. The criteria of the bands in the Raman spectra were made according to the literature [30-33] as shown in Table 5.

Table 4. Classification method of optical microscopic anisotropy component

Optical organization	Size (μm)		Aspect ratio
	Length	Width	
Mosaic structure	≤10	<10	
Small pieces structure	10~30	10~30	
Fine fiber structure	<30	<30	>5
Crude fiber structure	>30	>10	
Large structure	>30	>30	

Table 5. Raman bands and vibration modes reported in the literature [29-32]

Band	Raman shift (cm^{-1})	Vibration mode
G	1580	Ideal graphitic lattice (E_{2g}-symmetry)
D1	1350	Disordered graphitic lattice (graphene layer edges, A_{1g} symmetry)
D2	1620	Disordered graphitic lattice (surface graphene layers, E_{2g}-symmetry)
D3	1500	Amorphous carbon (Gaussian line shape)
D4	1200	Disordered graphitic lattice (A_{1g} symmetry), polyenes, ionic impurities

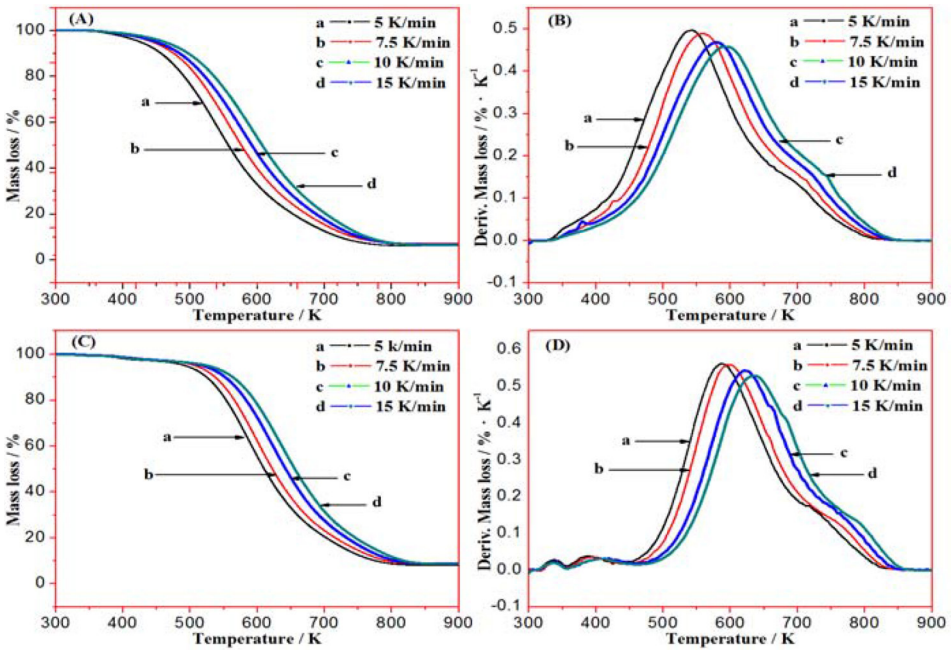

Fig. 1. TG/DTG curve of TS samples, (a, b) for TS-1, and (c, d) for TS-2.

Table 6. Decomposition data of TS from TG curves at various heating rates

α	β (K min^{-1})								E (KJ mol^{-1})			
	5		7.5		10		15		FWO method		KAS method	
	TS-1	TS-2	TS-1	TS-2	TS-1	TS-2	TS-1	TS-2	TS-1	TS-2	TS-1	TS-2
0.2	488.4	498.7	508.4	517.5	518.6	529.9	532.1	543.4	51.19	51.9	45.37	45.93
0.3	512.5	519.6	531.9	537.8	544.0	552.1	557.9	565.9	53.93	54.04	47.83	47.82
0.4	532.7	538.1	552.2	556.2	565.6	571.7	579.8	589.9	56.12	55.88	49.79	49.43
0.5	552.0	556.2	571.9	574.4	585.7	590.7	600.3	605.3	58.65	58.03	52.12	51.39
0.6	572.6	576.0	593.1	594.1	606.7	611.0	621.7	625.8	62.1	61.21	55.4	54.4
0.7	598.0	600.7	619.4	618.3	631.7	635.4	646.9	650.4	67.95	66.31	61.13	59.34
0.8	633.3	634.5	656.1	651.1	665.0	667.8	680.2	682.6	79.41	75.99	72.61	68.97

3. Results and Discussion

3.1. Thermogravimetric analysis results

The TG and DTG curves for TS at various heating rates (5, 7.5, 10, and 15 K min^{-1}) are shown in Fig. 1. With increase of the heating rate, the variation trends of the TG/DTG curves of TS-1 and TS-2 were similar, and the initial temperature and final temperature of thermal weight loss increased. The pyrolysis reaction rate was inferior to the added value of the heating rate during the thermo-gravimetric experiment. The initial weight loss temperature with the increase of heating rate. In addition, the maximum weight loss rate decreased with the increase of the heating rate. This phenomenon explains the increase of the heat polycondensation rate with the increase of the heating rate.

3.2. Activation energy calculated by FWO and KAS methods

The decomposition data and activation energy calculated by the FWO and KAS methods are listed in Table 6. As seen in Table 6, with increasing conversion, the activation energy slightly increased. However, the activation energy calculated by the FWO and KAS methods approached almost the exact same conversion. The results indicate that the activation energy values calculated by these methods were reasonable.

The average activation energy values calculated by the FWO and KAS methods was used to replace the pyrolysis activation energy values of samples. The average activation energy values of TS-1 and TS-2 are shown in Table 7. The average activation energy values of TS-1 and TS-2 were 58.12 KJ mol^{-1} and 57.19 KJ mol^{-1}, respectively.

Table 7. Pyrolysis activation energy values calculated by the FWO and KAS methods

Method	E (KJ mol^{-1})	
	TS-1	TS-2
FWO	61.34	60.48
KAS	54.89	53.90
Average	58.12	57.19

3.3. Kinetics parameters calculated by Satava-Sestak method

The activation energy and correlation coefficients for various reaction mechanisms (Table 3) were calculated by the Satava-Sestak method. According to the activation energy values calculated by the FWO and KAS methods, the reasonable mechanism function of TS-1 and TS-2 was the 15th thermal decomposition mechanism function, and the kinetic parameters are listed in Table 8. The activation energy values calculated by the Satava-Sestak method with the 15th thermal decomposition mechanism function were close to the average activation energy values calculated by the FWO and KAS methods, and the correlation coefficients (R^2) were more than 0.98, as seen in Table 8.

Therefore, it can be concluded that the decomposition mechanism of TS-1 and TS-2 is random nucleation and subsequent growth. The activation energy (E) and pre-exponential factor (A) of TS-1 were E = 54.39 KJ mol^{-1} and lgA = 7.10. Those of TS-2 were = 59.27 KJ mol^{-1} and lgA = 7.71. The thermal decomposition reaction of TS-1 and TS-2 had the same reaction series of 1.5. The pyrolysis reaction mechanism function of TS-1 and TS-2 can be expressed as $g(\alpha) = [-\ln(1-\alpha)]^{1.5}$. The pyrolysis kinetics equation of TS-1 and TS-2 are expressed as $\alpha^{1.5} = 1.26\times10^{7}\exp[54.39\times10^{3}/(8.314T)]t$ and $\alpha^{1.5} = 5.13\times10^{7}\exp[59.27\times10^{3}/(8.314T)]t$, respectively.

3.4. Polarized microscopic structure analysis of thermal conversion products

The polarized microscopic structure of TS-1-P and TS-2-P were studied by polarizing microscopy. The distribution of the optical anisotropic component was counted by lithofacies analysis software, and the judgment standard of optical anisotropic components are listed in Table 4. The results determined by polarizing microscopy are shown in Fig. 2. anisotropic component (d).

The optical anisotropic components of TS-1-P and TS-2-P were mainly composed of mosaic structure, fine fiber structure, and large structure (shown in Fig. 2). However, a comparison of these two samples shows that TS-1-P had greater contents of mosaic structure and large pieces structure than TS-2-P, and the content of fine fiber structure in TS-2-P was much higher than that in TS-1-P. This difference may be attributed to the source of the TS. Actually, TS-1 was obtained from modified pitch A, which was prepared by air oxidation treatment, and the O_2 par-

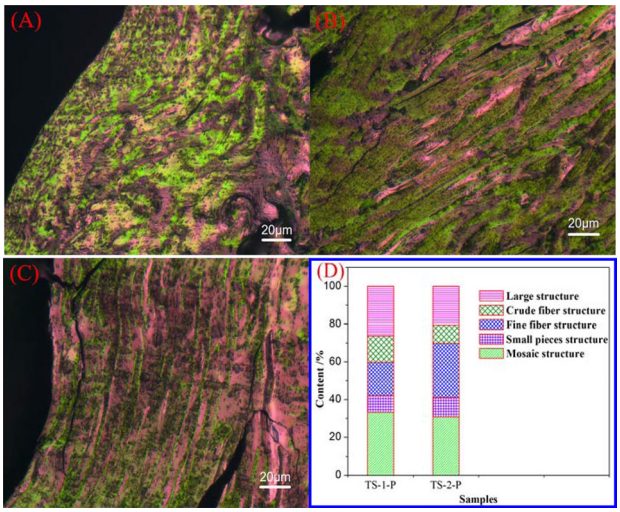

Fig. 2. Optical microstructures of calcined thermal conversion product (a-c); the distribution of optical anisotropic component (d).

Table 8. Kinetic parameter values calculated by the Satava-Sestak method

Sample	B (K min^{-1})	E (KJ mol^{-1})	lgA	R^2	n	E* (KJ mol^{-1})	(lgA)[a]
TS-1	5	50.62	6.70	0.991	1.5	54.39	7.10
	7.5	53.37	7.03	0.988	1.5		
	10	55.79	7.21	0.995	1.5		
	15	57.80	7.45	0.995	1.5		
TS-2	5	54.85	7.32	0.986	1.5	59.27	7.71
	7.5	59.17	7.71	0.986	1.5		
	10	60.39	7.79	0.990	1.5		
	15	62.65	8.02	0.990	1.5		

[a]Means for averaging.

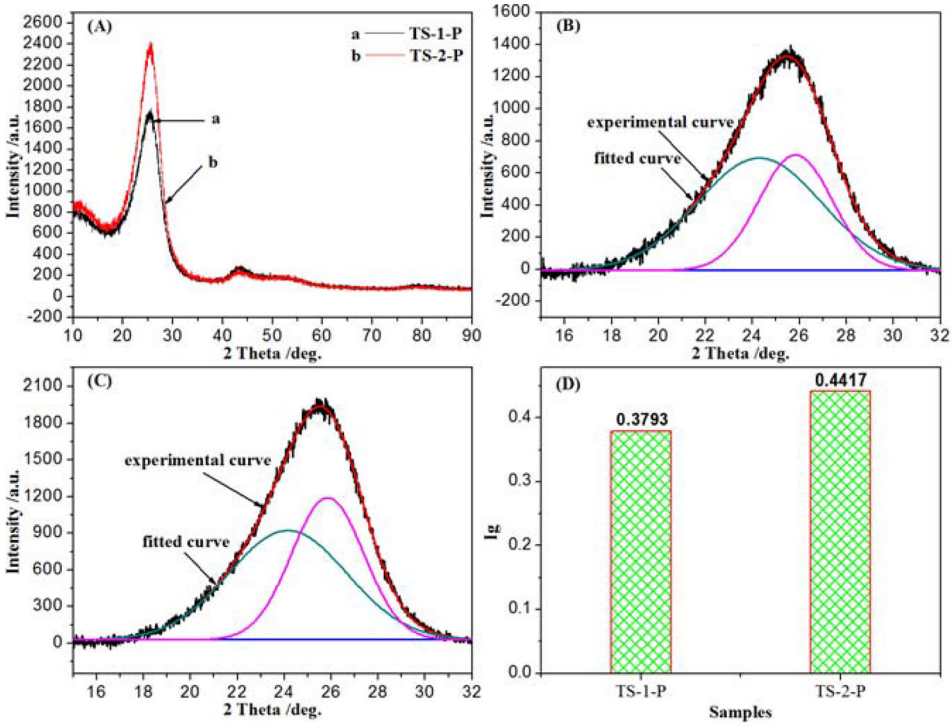

Fig. 3. XRD images of samples (a), curve-fitting images (b) and (c), and the distribution of Ig on samples (d).

ticipation in the system caused the oxidation linking reaction (this phenomenon is revealed in Table 2). The reaction of oxidation linking inhibits the formation of plane macromolecules in modified pitch A; therefore, TS-1-P has greater content of mosaic structure. In addition, TS-2 was obtained from modified pitch B. Modified pitch B was prepared by thermal polymerization in an inert atmosphere, and this reaction environment enabled the generation of plane macromolecules. As a result, the content of fine fiber structure in TS-2-P was obviously higher than that in TS-1-P.

3.5. XRD analysis results of thermal conversion products

The carbon crystalline structure of the calcined thermal conversion product from TS was examined by XRD analysis. The XRD patterns of the samples are shown in Fig. 3a. The variation trends of the XRD patterns of the two samples were similar, but the intensity of (002) was much higher in TS-2-P than in TS-1-P. Moreover, the width of (002) in TS-2-P was narrower than that in TS-1-P. This means that the micro-crystalline structure in TS-2-P was more ordered than that in TS-1-P.

The curve-fitting method was used for a better comparison of the micro-crystalline structure of the samples. As reported in [34], the broad hump of (002) of carbon material can be divided into two Gaussian peaks near 20 and 26° by peak-fitting, and these peaks are ascribed to the γ-band and π-band, respectively. The areas of the γ and π peaks are believed to be equal to the content of amorphous carbon and ideal graphite carbon. The content of ideal graphite carbon (Ig) can be calculated as:

$$Ig = A(\pi)/[A(\pi)+A(\gamma)] \quad (5)$$

where A(π) and A(γ) denote the areas of the π peak and γ peak, respectively, after peak-fitting.

The curve-fitted profile of calcined thermal conversion products from TS are shown in Fig. 3b and c, and the distributions of Ig on the samples are shown in Fig. 3d. Apparently, the amount of Ig in TS-2-P was higher than that in TS-1-P (Fig. 3d). This means that the content of ideal graphite carbon in TS-2-P was higher than that in TS-1-P. This result may be explained by the optical microstructure. As shown in Fig. 2d, the content of fine fiber structure in TS-2-P was much higher than that in TS-1-P, and the fine fiber structure in the carbonaceous materials indicated a graphite carbon structure.

3.6. Raman spectrum analysis of thermal conversion products

As shown in Fig. 4a, the two typical bands, the G band (graphite band) and D band (disorder band) were detected in the first-order region for the pyrolysis products. The Raman spectra obtained for TS-2-P had a much higher intensity than that of TS-1-P. To determine the carbon crystallite structure of the samples, the curve-fitting method was used to provide more information from the Raman spectral analysis results (Fig. 4b and c). The fitting standards refer to Table 5.

The band area ratios (I_G/I_T, I_D/I_T, and I_{D3}/I_G) were used to

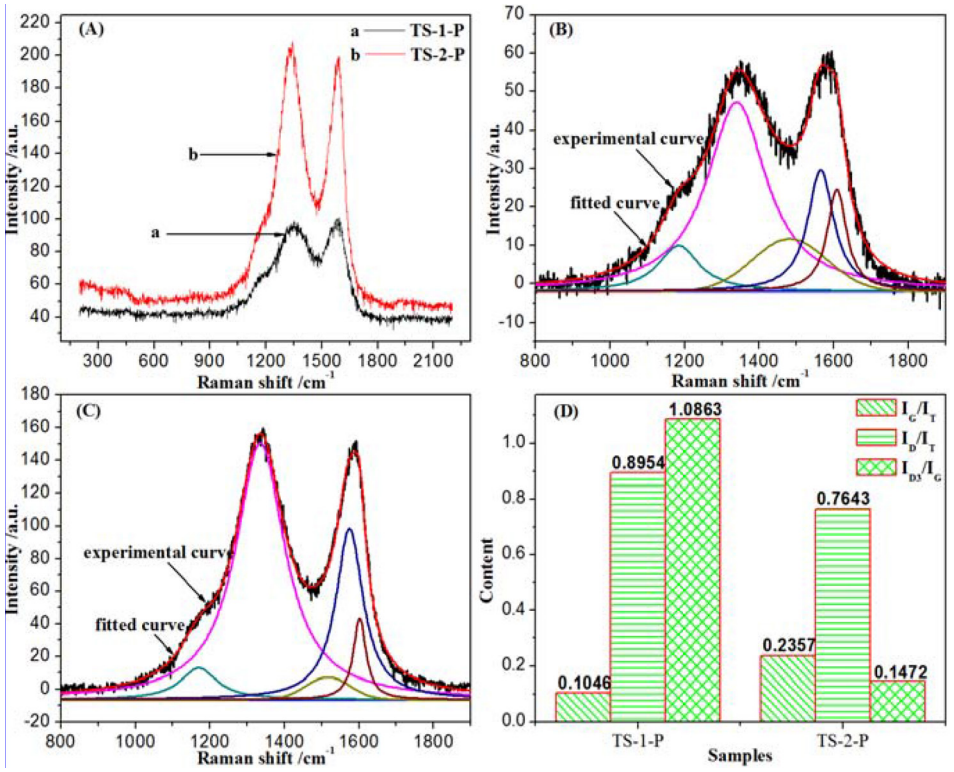

Fig. 4. Raman spectrum graph (a) and curve-fitting graphs (b, c); curve-fitting data of Raman spectrum from the sample.

measure the contents of the microcrystalline structures of the samples (Fig. 4d). It can be seen that the data (I_G/I_T) was higher in TS-2-P than in TS-1-P. On the contrary, I_D/I_T and I_{D3}/I_G in TS-1-P were obviously higher than in TS-2-P. This means that the well-ordered carbon structure content in TS-2-P was higher than that in TS-1-P. However, TS-1-P had a greater amorphous carbon content. This phenomenon is identical with the optical microstructure of these two pyrolysis products, and it is also consistent with the XRD analysis results.

4. Conclusions

The pyrolysis kinetics of TS was studied by the thermal analysis method. The activation energy values of TS-1 and TS-2 were calculated by the FWO and KAS methods according to the thermal conversion and temperature, and the activation energy of these two kinds of TS were 58.12 Kj mol^{-1} and 57.19 KJ mol^{-1}, respectively. The Satava-Sestak method was used to determine the pyrolysis kinetic parameters of the TS. The results reveals that the decomposition mechanism of TS-1 and TS-2 are the random nucleation and subsequent growth. The activation energy (E) and pre-exponential factor (A) of TS-1 were E=54.39 KJ mol^{-1} and lgA=7.10. The activation energy (E) and pre-exponential factor (A) of TS-2 were E=59.27 KJ mol^{-1} and lgA=7.71. The reaction series of TS-1 and TS-2 are 1.5. The pyrolysis reaction mechanism function of TS-1 and TS-2 can be expressed as $g(\alpha) = [-\ln(1-\alpha)]^2$. The pyrolysis kinetics equations of TS-1 and TS-2 are expressed as $\alpha^{1.5} = 1.26 \times 10^7 \exp[54.39\times10^3/(8.314T)]t$ and $\alpha^{1.5} = 5.13 \times 10^7 \exp[59.27\times10^3/(8.314T)]t$, respectively.

TS-1-P has greater contents of mosaic structure and large piece structure than TS-2-P, and the content of fine fiber structure in TS-2-P was much higher than that in TS-1-P in their optical microstructure. The amounts of Ig in TS-1-P and TS-2-P were 0.3793 and 0.4417 according to the XRD and curve-fitting results, respectively. The Raman spectrum and curve-fitting results showed that the content of well-ordered carbon structure in TS-2-P was higher than that in TS-1-P, and the TS-1-P had a higher amorphous carbon content.

Conflict of Interest

No potential conflict of interest relevant to this article was reported.

Acknowledgements

This work was supported by the National Natural Science Foundation of China (U1361126), the Specialized Research Fund for the Doctoral Program of Higher Education (20132120110001), and the Youth Fund of the Education Department of Liaoning Province (2017LNQN04).

References

[1] Ramjee S. Rand B, Focke WW. Low shear rheological behaviour of two-phase mesophase pitch. Carbon, **82**, 368 (2015). https://doi.org/10.1016/j.carbon.2014.10.082.

[2] Cao Q, Xie X, Li J, Dong J, Jin L. A novel method for removing quinoline insolubles and ash in coal tar pitch using electrostatic fields. Fuel, **96**, 314 (2012). https://doi.org/10.1016/j.fuel.2011.12.061.

[3] Bhatia G, Fitzer E, Kompalik D. Mesophase formation in defined mixtures of coal tar pitch fractions. Carbon, **24**, 489 (1986). https://doi.org/10.1016/0008-6223(86)90273-3.

[4] Murakam T, Nakaniwa M, Nakayama Y. Process for the preparation of super needle coke. US Patent 4,814,063 (1989).

[5] Sunago H, Migitaka W. Process for preparing needle coal pitch coke. US Patent 4,116,815 (1978).

[6] Mochida I, Yoon SH, Takano N, Fortin F, Korai Y, Yokogawa K. Microstructure of mesophase pitch-based carbon fiber and its control. Carbon, **34**, 941 (1996). https://doi.org/10.1016/0008-6223(95)00172-7.

[7] Yu B, Wang C, Chen M, Zheng J, Qi J. Two-step chemical conversion of coal tar pitch to isotropic spinnable pitch. Fuel Process Technol, **104**, 155 (2012). https://doi.org/10.1016/j.fuproc.2012.05.007.

[8] Yang Y, Wang C, Chen M. Preparation and structure analysis of nano-iron/mesocarbon microbead composites made from a coal tar pitch with addition of ferrocene. J Phys Chem Solids, **70**, 1344 (2009). https://doi.org/10.1016/j.jpcs.2009.07.023.

[9] Li S, Sun Q, Wang Y, Wu M, Zhang Z; College of Chemical Engineering; State Key Laboratory of Heavy Oil Processing; China University of Petroleum. Curing mechanism of condensed polynuclear aromatic resin and thermal stability of cured resin. China Pet Process Petrochem Technol, **2015**, 9 (2015).

[10] Wu M, Wang Y, Jiang W, Li S, Sun Q, Zheng J, Qiu J. Improvements of heat resistance and adhesive property of condensed polynuclear aromatic resin via epoxy resin modification. Pet Sci, **11**, 578 (2014). https://doi.org/10.1007/s12182-014-0374-x.

[11] Wu M, Shi Y, Li S, Wang Y, Tan M, Wang D, Zheng J, Tsubaki N. Synthesis and characterization of condensed polynuclear aromatic resin derived from ethylene tar. China Pet Process Petrochem Technol, (4), 42 (2012).

[12] Wu MB, Shi YY, Li SB, Guo N, Wang YW, Zheng JT, Qiu JS. Synthesis and characterization of condensed poly-nuclear aromatic resin using heavy distillate from ethylene tar. New Carbon Mater, **27**, 469 (2012). https://doi.org/10.1016/S1872-5805(12)60027-4.

[13] Fernández JJ, Figueiras A, Granda M, Bermejo J, Menéndez R. Modification of coal-tar pitch by air-blowing. I. Variation of pitch composition and properties. Carbon, **33**, 295 (1995). https://doi.org/10.1016/0008-6223(94)00130-R.

[14] Zeng SM, Maeda T, Tokumitsu K, Mondori J, Mochida I. Preparation of isotropic pitch precursors for general purpose carbon fibers (GPCF) by air blowing. II. Air blowing of coal tar, hydrogenated coal tar, and petroleum pitches. Carbon, **31**, 413 (1993). https://doi.org/10.1016/0008-6223(93)90128-W.

[15] Barr JB, Lewis IC. Chemical changes during the mild air oxidation of pitch. Carbon, **16**, 439 (1978). https://doi.org/10.1016/0008-6223(78)90090-8.

[16] Lewis IC. Thermal polymerization of aromatic hydrocarbons. Carbon, **18**, 191 (1980). https://doi.org/10.1016/0008-6223(80)90060-3.

[17] Mora E, Santamaría R, Blanco C, Granda M, Menéndez R. Mesophase development in petroleum and coal-tar pitches and their blends. J Anal Appl Pyrolysis, **68-69**, 409 (2003). https://doi.org/10.1016/S0165-2370(03)00034-2.

[18] Oh SM, Park YD. Comparative studies of the modification of coal-tar pitch. Fuel, **78**, 1859 (1999). https://doi.org/10.1016/S0016-2361(99)00093-9.

[19] Petrova B, Budinova T, Petrov N, Yardim MF, Ekinci E, Razvigorova M. Effect of different oxidation treatments on the chemical structure and properties of commercial coal tar pitch. Carbon, **43**, 261 (2005). https://doi.org/10.1016/j.carbon.2004.09.006.

[20] Knight SA. Analysis of aromatic petroleum fractions by means of absorption mode carbon-^{13}N.M.R. Spectroscopy. Chem Ind, **11**, 1920 (1967).

[21] Clutter DR, Petrakis L, Stenger RL, Jensen RK. Nuclear magnetic resonance spectrometry of petroleum fraction: carbon-13 and proton nuclear magnetic resonance characterizations in terms of average molecule parameters. Anal Chem, **44**, 1395 (1972). https://doi.org/10.1021/ac60316a002.

[22] Huang X, Kocaefe D, Kocaefe Y, Bhattacharyay D. Interaction of bio-coke with different coal tar pitches. Fuel, **179**, 179 (2016). https://doi.org/10.1016/j.fuel.2016.03.058.

[23] Öner FO, Yürüm A, Yürüm A. Structural characterization of semicokes produced from the pyrolysis of petroleum pitches. J Anal Appl Pyrolysis, **111**, 15 (2015). https://doi.org/10.1016/j.jaap.2014.12.023.

[24] Ren H, Chen Z, Wu Y, Yang M, Chen J, Hu H, Liu J. Thermal characterization and kinetic analysis of nesquehonite, hydromagnesite, and brucite, using TG–DTG and DSC techniques. J Therm Anal Calorim, **115**, 1949 (2014). https://doi.org/10.1007/s10973-013-3372-0.

[25] Tahmasebi A, Kassim MA, Yu J, Bhattacharya S. Thermogravimetric study of the combustion of Tetraselmis suecica microalgae and its blend with a Victorian brown coal in O_2/N_2 and O_2/CO_2 atmospheres. Bioresour Technol, **150**, 15 (2013). https://doi.org/10.1016/j.biortech.2013.09.113.

[26] Muraleedharan K. Thermal decomposition kinetics of potassium iodate. Part II: Effect of gamma-irradiation on the rate and kinetics of decomposition. J Therm Anal Calorim, **114**, 491 (2013). https://doi.org/10.1007/s10973-013-3034-2.

[27] Tian L, Tahmasebi A, Yu J. An experimental study on thermal decomposition behavior of magnesite. J Therm Anal Calorim, **118**, 1577 (2014). https://doi.org/10.1007/s10973-014-4068-9.

[28] Škvára F, Šesták J. Computer calculation of the mechanism and associated kinetic data using a non-isothermal integral method. J Therm Anal, **8**, 477 (1975). https://doi.org/10.1007/BF01910127.

[29] Rongzu H, Zhengquan Y, Yanjun L. The determination of the most probable mechanism function and three kinetic parameters of exothermic decomposition reaction of energetic materials by a. Thermochim Acta, **123**, 135 (1988). https://doi.org/10.1016/0040-6031(88)80017-0.

[30] Morga R, Jelonek I, Kruszewska K, Szulik W. Relationships between quality of coals, resulting cokes, and micro-Raman spectral characteristics of these cokes. Int J Coal Geol, **144-145**, 130 (2015). https://doi.org/10.1016/j.coal.2015.04.006.

[31] Sadezky A, Muckenhuber H, Grothe H, Niessner R, Pöschl U. Raman microspectroscopy of soot and related carbonaceous materials: spectral analysis and structural information. Carbon, **43**, 1731

(2005). https://doi.org/10.1016/j.carbon.2005.02.018.
[32] Morga R. Micro-Raman spectroscopy of carbonized semifusinite and fusinite. Int J Coal Geol, **87**, 253 (2011). https://doi.org/10.1016/j.coal.2011.06.016.
[33] Beyssac O, Goffé B, Petitet JP, Froigneux E, Moreau M, Rouzaud JN. On the characterization of disordered and heterogeneous carbonaceous materials by Raman spectroscopy. Spectrochim Acta Part A, **59**, 2267 (2003). https://doi.org/10.1016/S1386-1425(03)00070-2.
[34] Manoj B, Kunjomana AG. Study of stacking structure of amorphous carbon by X-ray diffraction technique. Int J Electrochem Sci, **7**, 3127 (2012).